



HAL
open science

3D-printed electroactive polymer force-actuator for large and high precise optical mirror applications

Kritsadi Thetpraphi, Waroot Kanlayakan, Suphita Chaipo, Gil Moretto, Jeff Kuhn, David Audigier, Minh Quyen Le, Pierre-Jean Cottinet, Lionel Petit, Jean-Fabien Capsal

► To cite this version:

Kritsadi Thetpraphi, Waroot Kanlayakan, Suphita Chaipo, Gil Moretto, Jeff Kuhn, et al.. 3D-printed electroactive polymer force-actuator for large and high precise optical mirror applications. Additive Manufacturing, 2021, 47, pp.102199. 10.1016/j.addma.2021.102199 . hal-03662250

HAL Id: hal-03662250

<https://hal.science/hal-03662250v1>

Submitted on 16 Oct 2023

HAL is a multi-disciplinary open access archive for the deposit and dissemination of scientific research documents, whether they are published or not. The documents may come from teaching and research institutions in France or abroad, or from public or private research centers.

L'archive ouverte pluridisciplinaire **HAL**, est destinée au dépôt et à la diffusion de documents scientifiques de niveau recherche, publiés ou non, émanant des établissements d'enseignement et de recherche français ou étrangers, des laboratoires publics ou privés.



Distributed under a Creative Commons Attribution - NonCommercial 4.0 International License

3D-Printed Electroactive Polymer Force-Actuator for Large and High Precise Optical Mirror Applications

Kritsadi Thetraphi¹, Waroot Kanlayakan^{1#}, Suphita Chaipo^{1#}, Gil Moretto², Jeff Kuhn³, David Audigier¹, Minh Quyen Le¹, Pierre-Jean Cottinet¹, Lionel Petit¹, and Jean-Fabien Capsal^{1*}

¹ Univ Lyon, INSA-Lyon, LGEF, EA682, F-69621, Villeurbanne, France

² Centre de Recherche Astrophysique de Lyon (CRAL), 9 avenue Charles André, 69230 Saint-Genis-Laval, France

³ University of Hawaii's Institute for Astronomy, 34 Obia Ku St, Pukalani, Maui, HI, USA

Master Degree Internships between INSA/Lyon and Prince of Songkla University, Songkhla, Thailand.

* Corresponding author: jean-fabien.capsal@insa-lyon.fr; Tel.: +33-4 72 43 88 33

Abstract:

We describe a new development for a full 3D-printed-force actuator based on an advanced electroactive polymer (EAP) dedicated to large and live optical mirror applications, i.e., Live-Mirror Project (<https://www.planets.life/live-mirror>). The thin-film casting method was used to additively manufacture actuators, and we developed an integrating 3D printing technology to the EAP force-actuator production. Our 3D-printed actuator consists of the plasticized terpolymer layer (polyvinylidene fluoride-trifluoroethylene-chlorotrifluoroethylene (PVDF-TrFE-CTFE) doped with diisononyl phthalate (DINP) plasticizer) sandwiched between two electrodes layers made of conductive terpolymer carbon black (CB) composite. The conductive CB layers were developed here to have a high electrical conductivity that can be used under significant voltage. We also made compatible blends with an actuator layer based on DINP polymer. Several fully 3D-printed EAP proof-of-concept actuator configurations were printed on a two-millimeters thick flat glass, i.e., an optical mirror surface. Its electromechanical performance was analyzed as a function of actuator volume, layer number, and electrical field intensity.

Keywords: Electroactive doped polymer, 3D printing, EAP force-actuator, active optical mirror, active control of glass deformation, flexible printed materials, optimization of printed electrodes.

I. Introduction

3D printing technology offers several advantages for diverse materials processing such as rapid prototyping making use of an object from a computer-aided design (CAD). Additive manufacturing developments have improved and advanced 3D-printer technology by providing commercially customized products to overcome the time-consuming process of complex shape products [1,2]. In particular, *flexible printed materials* have been attractive for large-area electronic devices, e.g., wearable electronics of 3D tactile sensors [3,4], printed CNC (Computerized Numerical Control) process scaffolds for specific cell integration [5], polymer photo-detectors [6], and 3D-printed soft dielectric elastomer actuators [7,8].

Material extrusion printing is a common technique used to build a structure of any desired shape of dielectric elastomer [9]. This 3D printing process allows various kinds of material to be extruded to build up a platform along a predetermined path. The difficulty of this printing technique is the use of a fluid or solution-based material that requires the control of a variety of parameters that characterize the material/solvent: evaporation rate, viscosity grade, flow regulation, mold temperature, chemical compatibility for multi-material structure. These must be tuned to achieve an efficient and reproducible printing process. We recently reported the possibility of using a casting method to produce an EAP-based modified terpolymer as a force-actuator system for a highly accurate optical surface deformation and correction [10,11].

45 To fabricate active optics in Live-Mirror applications, we used the EAP that can shape and/or
46 deform the mirror surface thanks to its electromechanical conversion. Recently, Thetraphi *et al.* [11]
47 reported a handcrafted prototype [11], i.e., a film-casting actuator production. The design is a shear actuator
48 (thin-film EAP glued with a single glass plate). To develop a unique force-actuator device that can be
49 precisely integrated into certain mirror positions, we opted for an extrusion-based 3D printing technique
50 through Hyrel System 30M 3D printer [12]. Based on this approach, it is possible to overcome the interface-
51 related problems, which principally caused by a deficiency in force transferring between EAP to a glass
52 surface (handcrafted prototype). Considering the customized electrode and actuator patterns, it is necessary
53 to design each actuator matching individual optical surfaces. Thus, the integration of additive manufacturing
54 is very important to fabricate a large area, unique and precise actuator to fulfill the requirement of the future
55 Live-Mirror application. Additionally, the provision of extrusion-based 3D printing techniques will be
56 essential for developing a wide range of smart mirror fabrication. In other words, a specified actuator shape
57 is needed to accurately integrate it into certain mirror positions, from small-scale (lab-scale) to wide-reaching
58 innovative applications. In this paper, we aim to fabricate a force-actuator using 3D printing technology
59 and optimize its electromechanical performance with several configurations. The main purpose involves
60 demonstrating the proof-of-concept of 3D printing multilayer EAP included with customized electrodes.
61 Although researchers are actively investigating 3D printing technology, the full-printed actuator is still
62 rather limited today because of incompatibility between polymer and electrode layers [1,7,13].

63 3D printing of the conductive electrode layer is the most challenging. Most conductive metallic
64 inks require a sintering process to reach a good conductive range and bulk content. The sintering procedure
65 of some conductive inks, e.g., silver ink, is 150°C and above. Nonetheless, stretchable electronic
66 applications need to be fabricated at moderate temperatures to prevent sample damage and/or degradation
67 of the incorporated materials. Dearden *et al.* [14] demonstrated the possibility of reducing the sintering
68 temperature of organometallic inks lower than 150°C. Another option to avoid operating materials under
69 high temperatures is to use intrinsically conductive polymer (ICP) and/or conductive polymer composite
70 (CPC). Even though ICP and CPC exhibit lower conductivity than metallic ink, their advantages in terms
71 of compliance, cost, resilience, density, and biocompatibility have attracted a great deal of research interest.

72 Recent studies have focused on the improvement of electrical conductivities of ICP and CPC for
73 flexible actuator and sensor applications. Kayser *et al.* [15] described a stretchable scaffold made from an
74 intrinsically synthesizing variant of PEDOT: PSS to develop soft and skin-like semiconductors and
75 conductors. Cochrane *et al.* [16] used the evoprene 007 (EVO) ($T_m \approx 82^\circ\text{C}$) for polymer hosts filled with
76 carbon black (CB) powder as a smart flexible sensor. Kumar *et al.* [17] reported on an elastomer ethylene-
77 vinyl acetate EVA ($T_m \approx 75^\circ\text{C}$) doped with graphite and CNC-assisted manipulated as a three-dimensional
78 flexible electrically conductive structure for soft robotics applications. Hence, ICP and CPC could intimate
79 the printability to mitigate solvent evaporation under low temperature showing their high potential in
80 applications of soft electronic devices. Numerous parameters must be considered to demonstrate the
81 printability of materials in additive manufacturing, e.g., compatibility between conductive inks and substrate
82 or cooperative materials, wettability (substrate-polymer), surface bonding (polymer-polymer), curing
83 temperature, etc. Considering all such challenging complexities, we developed here a conductive ink made
84 from P(VDF-TrFE-CTFE) fluorinated terpolymer doped with CB nanoparticles (Vulcan® XC72R) that is
85 adaptable for extrusion 3D printing.

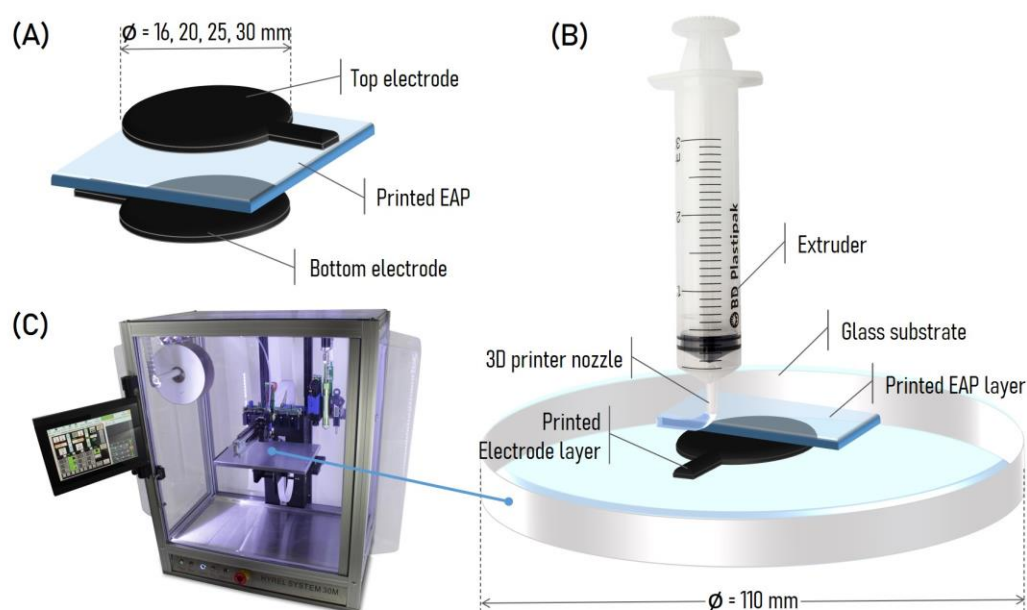
86

87 II. Fabrication process and method of characterization

88 i. Material design and 3D printing setup

89 The EAP solution is prepared in a liquid form ready for printing by dissolving terpolymer granules
90 in methyl ethyl ketone (MEK, also known as butanone) solvent at a fraction of 20.25% wt. The fully printed
91 force-actuator proof of concept includes the 3D printing of all layers, i.e., consisting of the EAP plasticized
92 terpolymer sandwiched between the two terpolymer/CB composite (top and bottom) layers. Figure 1
93 shows the extrusion-based 3D printing setup: (A) the electrode circular-shaped layers are printed with
94 different diameters, and the EAP layer is designed to have a larger area than the electrode ones to avoid
95 electrical arcing between these electrodes under high voltage; (B) the material extrusion setup consisted of
96 a modular head sterile cold flow (SDS) [12] extruders (at room temperature); and (C) a glass platform that
97 allowed translation in x-, y-, and z-directions. Here, we used commercial float glasses with 110mm-diameter
98 and 2mm-thickness as the optical substrate. The mechanical properties of the glass are found on [18]. In
99 the preparation process, the actuator was printed on one side of the glass (called “back surface”) while the
100 other side was referred to as the control optical surface (called “front surface”). The front surface of the
101 glass coated with a gold layer of 25nm thick allows obtaining its deformation measurement. On the other
102 hand, this architecture prevents the reflection from the back surface of the glass. Consequently, the optical
103 properties of EAP would not much affect the glass deformation, which is therefore not taken into
104 consideration for the mirror application.

105 The extruder used in this work allows the use of sterile syringes at room temperature. The prepared
106 solution was put in a syringe and printed at room temperature with a speed of 800 mm/min through a
107 nozzle of 14G for the EAP, and 18G for the electrode. Using a smaller nozzle for printing electrodes leads
108 to higher pattern precision, particularly in the case of complex shapes. Whatever actuator dimension, the
109 printing configuration was carried out with 100% filling density in order to achieve the best material
110 performance. To completely evaporate the solvent from the full-printed actuator (consisting of three layers
111 of electrode/EAP/electrode), samples were put into an oven with temperature-controlled of 102°C for 2h,
112 then cooled down slowly for 16h to room temperature. The average thickness of the whole sample is
113 approximately 130 μm including 90-100 μm for the EAP layer and 15-20 μm for the electrode circular-
114 shaped layer. A control-software 3D printing code (Repetrel by Hyrel [12]) is used to control parameters
115 such as tuning, speed, and pressure. This allows one to print the EAP force-actuator in optimized
116 configurations similar to those in a COMSOL simulation.



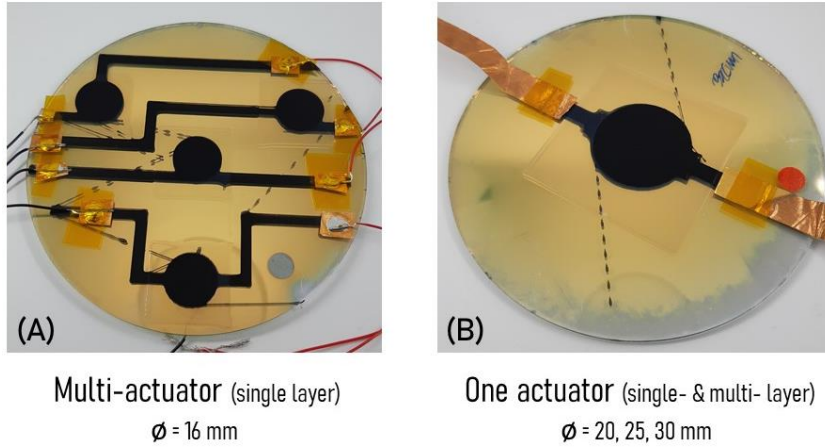
117

118 **Figure 1.** The full-printed actuator based EAP: (A) force-actuator made of plasticized terpolymer switched between two electrodes layers
 119 of terpolymer/ CB composite; (B) 3D printing setup of actuator layers using (C) the commercial System 30M Hyrel 3D printer [12].

120 Thetraphi *et al.* [10,11,19] demonstrated the high potential of the stacked multilayer actuator
 121 configuration, which successfully enhances the dielectric properties as well as the electromechanical
 122 coupling of the EAP materials. Here, a stacked actuator consisting of three printed layers (i.e., one active
 123 layer based EAP and two electrode layers-based conductive-ink) was investigated corresponding to layer-
 124 by-layer extrusion (Figure 1B). Printed electrodes with a conductive polymer ink revealed their high
 125 potential to implement flexible and stretchable electronic devices such as nanoparticles colloid suspension,
 126 organometallic inks, carbon nanotube, graphene oxide, and reactive inks [20].

127 The first full-printed EAP prototype was fabricated on a single glass blank working in a shear-
 128 mode actuator under various configurations. Such a single-layer actuator consists of a single EAP layer
 129 (terpolymer doped 8 wt%DINP), and two electrode layers (terpolymer doped 5wt% CB composite). Figure
 130 2 shows two different shear prototype configurations: (1) the full-printed multi-actuator prototype has four
 131 individual single-layer actuators as shown in Figure 2A; (2) the full-printed single actuator prototype has
 132 one actuator located at the central glass substrate (Figure 2B).

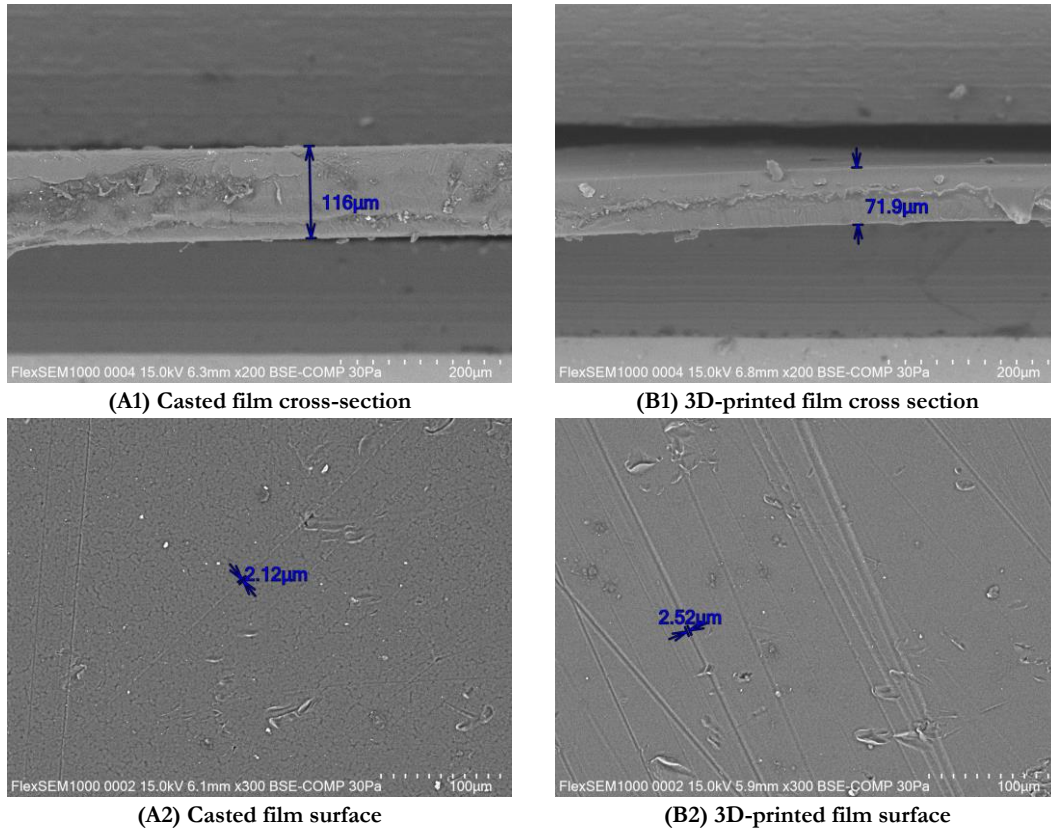
133 Since the 3D printing process is somehow analog to the thin-film casting method, we presumed
 134 that the surface roughness of samples made by the new 3D technique is relatively smooth and thus would
 135 not much affect the actuator performance. Indeed, both methods lead to a fabrication of thin film in which
 136 the EAP and/or the electrode were fully coated on the glass substrate without any intermediary adhesive
 137 layer. The SEM images (FlexSEM 1000II) illustrating the surface roughness of those samples fabricated by
 138 3D printing or casting process are presented in Figure 3. The morphological observations of the film surface
 139 in both techniques are homogeneous and undifferentiated. As observed in Figure 3 (A2) and (B2), few tiny
 140 straight lines of $\sim 2\mu\text{m}$ -width appear over both film surfaces, which is possibly originated from some
 141 inevitable defects during the elaboration process.



142

143 **Figure 2.** The full-printed actuator prototype: (A) Multi-actuator configuration consisting of four actuators with a 16-mm-diameter
 144 electrode; and (B) single actuator at the central mirror glass which has three different electrodes sizes. The single actuator is printed as a
 145 multilayer stacked actuator by successively depositing 3 layers of electrode/EAP/ electrode.

146



147 **Figure 3.** SEM micrographs of plasticized terpolymer thin films prepared by (A1-2) film casting method, and (B1-2) 3D-printed
 148 method.

149

ii. Electrical characterization of CB electrode layers

150

151

152

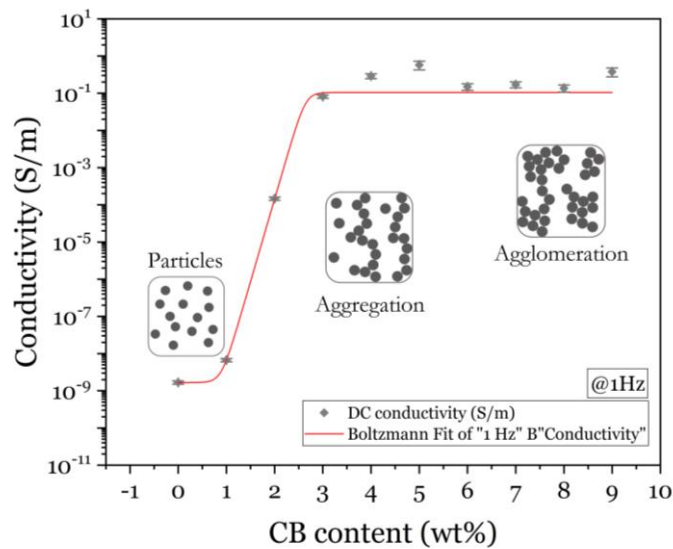
153

154

Here a conductive polymer composite (CPC) was selected to print the two electrode layers of the actuator design (Figure 1A). This approach uses the same polymer host between the electrode and EAP actuator layer. It reduces the complexity of ink preparation and avoids material compatibility issues. Because the deformation needed to shape the mirror is less than 1%, we exclusively focus on the linear elastic domain [21] of the terpolymer in this investigation. Based on the linear stress/strain curve characterized in

our previous work [22], it is possible to deduce the Young modulus of the plasticized terpolymer, i.e. approximately 30 MPa. This property is perfectly suitable for dedicated optical applications. Indeed, the EAP is flexible enough to deform itself, but it is somehow strong enough to generate sufficient force to shape the mirror. A compromise between force and deformation makes terpolymer one of the most appropriate choices for the design of actuator devices [21]. It is worth noting that the low percentage of CB powder dispersed into the terpolymer matrix would not significantly modify its Young modulus. For more details about the mechanical properties of terpolymer composites doped with different DINP or CB fraction content, the readers can refer to [11,23–25].

The CB particles were well-dispersed in the Terpolymer/MEK solution thanks to an ultrasonic probe (UP400S from Hielscher). Figure 4 outlines the S-shaped electrical conductivity of the printed Terpolymer/CB ink with different weight fractions of CB particles. Beyond 1 wt% of CB content, the conductivity drastically increases confirming that the percolation threshold of the composite is approximately 4 -5 wt%. At 5 wt% of CB filler, the electrode layer became conductive and reached a small overshoot of 0.57 ± 0.14 S/m. Beyond the percolation transition, the conductivity of the composite ink somehow dropped and was in the saturation regime. Such a slight decrease in the electrical conductivity can be explained by the fact that higher CB concentration probably generated a cluster of particle agglomeration, leading to reduced efficacy in the conductive pathway. All these experimental results indicate that the transition from insulation polymer to high conductivity composite depends on the formation of an interconnected conductivity network. In other words, superior conductivity arises from the high dispersion and the formation of a network structure in the polymer matrix. It can be concluded that many factors comprising intrinsic electrical properties of the doped particles, aspect ratio, dispersion state, and contact resistance between particle/particle and particle/matrix might greatly affect the electrical conductivity of the whole composites [26,27].

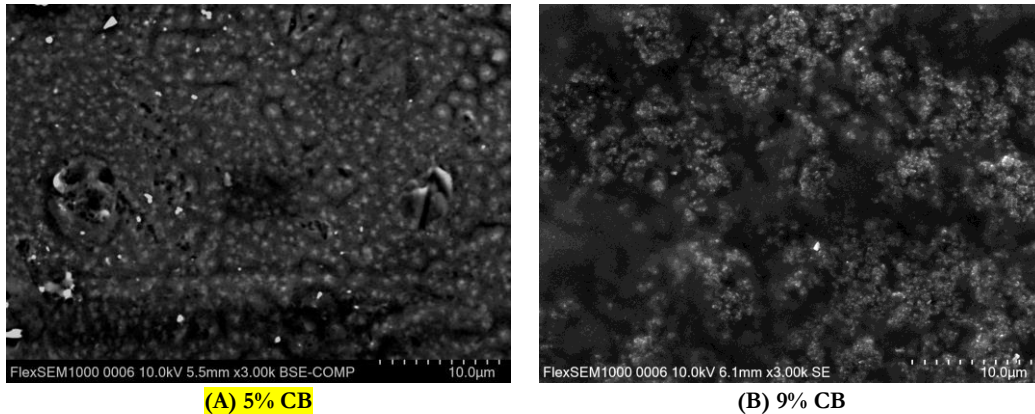


178
179 **Figure 4.** The electrical conductivity of terpolymer filled with carbon black (CB) particles accurately obtained from the dielectric broadband
180 spectroscopy (DBS) system operated at a sinusoidal voltage of 1V amplitude and 1 Hz frequency.

181 Considering the dispersion of CB particles in the polymer matrix, Figure 5 presents micrograph
182 images via scanning electron microscope (SEM, FlexSEM 1000II) analysis of samples elaborated with 5%
183 and 9% of CB concentration. A higher agglomeration of CB particles is observed on the 9% composite,
184 which is consistent with the fact that its electrical conductivity is lower than the one of the 5%. To some
185 extent, the conductivity slightly increases again at 9%, i.e., maybe due to measurement uncertainties and
186 random particle formation in the conductivity network.

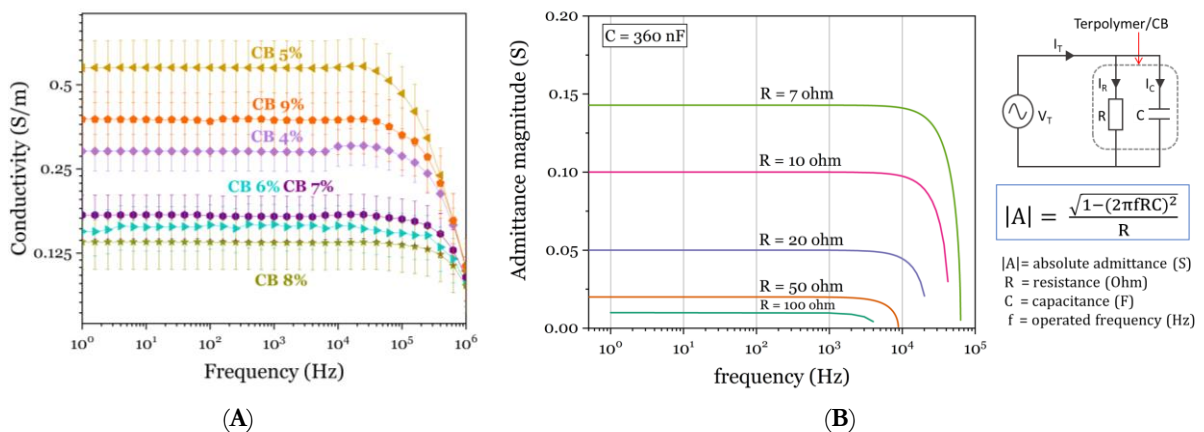
187 Controlling cluster formation of CB composite above percolation is complex, especially when
 188 particles are dispersed randomly. In this study, we demonstrated that the electrical conductivity of the
 189 printed electrodes is sufficient for a satisfying actuation response. Due to the low operating frequency, the
 190 EAP has such a high electrical impedance as compared to the electrodes. Finally, the 5wt% of CB composite
 191 is the most favorable material to be used as the printable electrode, because of its homogeneous dispersion
 192 in the polymer host, as well as its good electrical conductivity at the low percentage of doping filler.
 193 Furthermore, the 5wt% EAP layer somehow remains a relatively low Young modulus with respect to the
 194 9% counterpart [23,25,28].

195



196 **Figure 5.** SEM micrographs of the terpolymer doped with CB (A) 5wt% and (B) 9wt% respectively. Compared to the 5% CB
 197 concentration, the 9% counterpart seems to provide a larger cluster of CB particle agglomeration, creating the disconnected path within the
 198 polymer matrix.

199 Figure 6A shows the electrical conductivity evolution of CB composite above the percolation
 200 regime in a large frequency range of [1 Hz, 1 MHz]. Whatever the weight fraction of CB powders, the
 201 conductivity values are stable under low frequencies while being dropped over high frequencies of around
 202 10^5 Hz. Despite this non-perfect conductive behavior, the terpolymer/CB composite remains an interesting
 203 solution for 3D printing electrodes because of its good conductivity and high adaptability to the EAP
 204 actuator layer.



205 **Figure 6.** The electrical conductivity of terpolymer doped with CB composite above the percolation region characterized as a function of
 206 frequency: (A) the experimental characterization measured with Solartron; and (B) the admittance $|A|$ evaluation calculated through
 207 the real capacitance and the resistance values of terpolymer/CB composite-based RC parallel circuit.

208 The polymer composite is a capacitive-like material that could be modeled as an RC parallel circuit
 209 [29,30]. Its admittance value \mathbf{A} (Siemen: S) is determined according to Figure 6B. Similar to the conductivity
 210 property, the admittance magnitude is also frequency-dependent where a significant fall has been observed

211 under high frequencies. The identification between the experimental data and the analytical model of the
212 EAP's admittance allows us to predict the RC components of the terpolymer doped with high CB
213 concentration (4%-9% by mass). The estimated resistance and capacitance of the 64 μm -thick films are
214 approximately 2-10 ohms and 360 nF, respectively.

215 The conductivity evolution is given by the experimental measurement (Figure 6A) and the theoretical
216 modeling (Figure 6B). It behaves as a low-pass filter response where the cut-off frequency is around 73 ± 5
217 kHz. The small discrepancy between experiment and model is possibly due to the composite particle
218 agglomeration, which provides an inconsistent resistance value to the material composite. Here, we operate
219 the polymer actuator in a low-frequency range (lower than 50 mHz), which is compliant to large and
220 accurate optical active surface mirror low-frequency correction and not a high bandwidth requirement. This
221 means that the effect of the AC filter at a very high-frequency range could be neglected (at least for this
222 application).

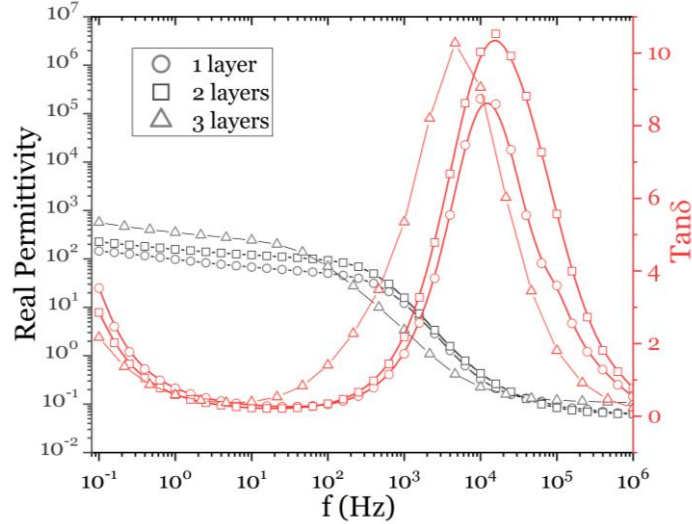
223 The main goal here is to achieve active shape control with many-degree-of-freedom force actuators
224 created by an additive 3D printing-based technology. Based on an optimized EAP force actuator system in
225 a sandwich of specified shaped/slumped glass surfaces, it is possible to create a novel actively controlled
226 **hybrid meta-material** with a superior stiffness-to-density ratio dedicated to optical quality mirror surfaces.

227 **iii. Dielectric characterization of force Actuators**

228 The dielectric permittivity is one of the most important intrinsic parameters of an EAP. A higher
229 dielectric constant implies a higher efficiency of the mechanical energy density for actuation performance
230 [21]. The full-printed actuator ability was assessed by their dielectric characterization as a function of
231 frequency. Figure 7 illustrates the relative permittivity real part (ϵ_r) as well as the loss factor (**Tan δ**) of the
232 modified terpolymer under a large frequency range of 0.1 Hz – 1 MHz. When the DINP plasticizer is
233 incorporated within the terpolymer matrix, it strongly promotes the mobility of dipolar relaxation and thus
234 enhances the dielectric permittivity [22,24,31]. However, too much DINP quantity could decrease the
235 electrical strength of the blend producing dielectric breakdown. Thetraphi *et al.* [11] reported that the
236 terpolymer must be integrated with an 8-10 wt% plasticizer to get the best trade-off between the dielectric
237 property and the breakdown strength. Here, terpolymer doped with 8 wt % DINP was employed. Figure 7
238 shows that the full-printed multilayer actuator leads to substantial enhancement in dielectric permittivity
239 concerning the neat terpolymer ($\epsilon_r \sim 70$), i.e., 150 for the single-layer actuator and 450 for the three-layer
240 actuator, respectively.

241 Another key parameter relating to actuator performance is dielectric loss. As indicated in Figure 7,
242 the resulting loss tangent of the fabricated composite is relatively high, which might originate from the low
243 conductivity (higher resistivity) of the printed electrode layers. Our printed electrodes are not perfectly
244 conductive versus an ideal electrode (e.g., one made of gold or copper). This is because their conductivity
245 (i.e. 0.5 S/m shown in Figure 4) is the same order of magnitude as that of typical semiconductors like Si
246 and Ge. The actuator with high losses can be minimized by improving the conductivity of the printed
247 electrode. Live-Mirror systems are operated at very low frequency (~ 50 mHz), and the loss issue at high
248 frequency can be neglected. In contrast, the loss is principally generated by the Ohmic conduction
249 mechanism under a quasi-static regime as in our application [32]. Pedroli *et al.* proposed a different approach
250 to reducing the conduction loss effect in the EAP. This matter will be considered in future studies to
251 improve the conductive property of our printed electrode.

252



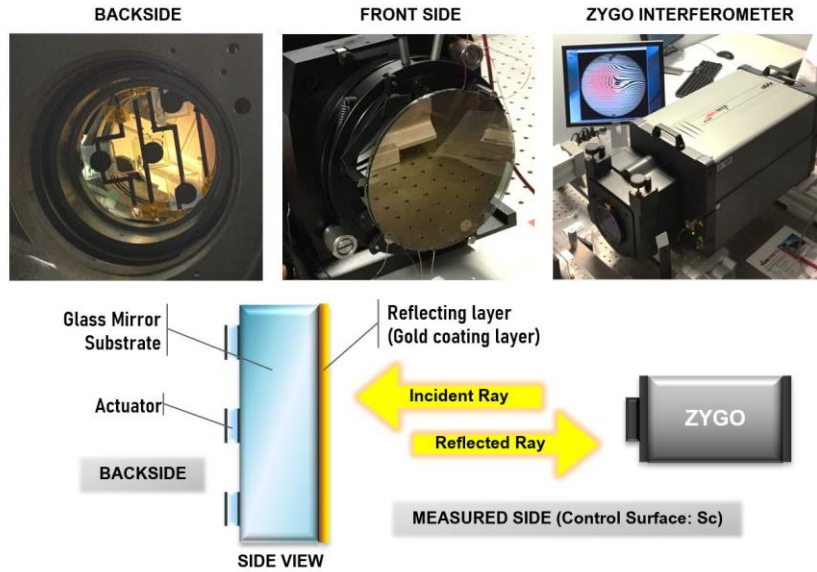
253

254 *Figure 7. The dielectric broadband spectroscopy of full-printed EAP with different layers operated under a sinusoidal voltage of $1V_{AC}$ -*
 255 *amplitude at room temperature. The gray curves are related to the real permittivity while the red curves are dedicated to the $\tan\delta$ losses.*

256

257 III. Customized Full Printed Force-Actuator — Live Mirror Application

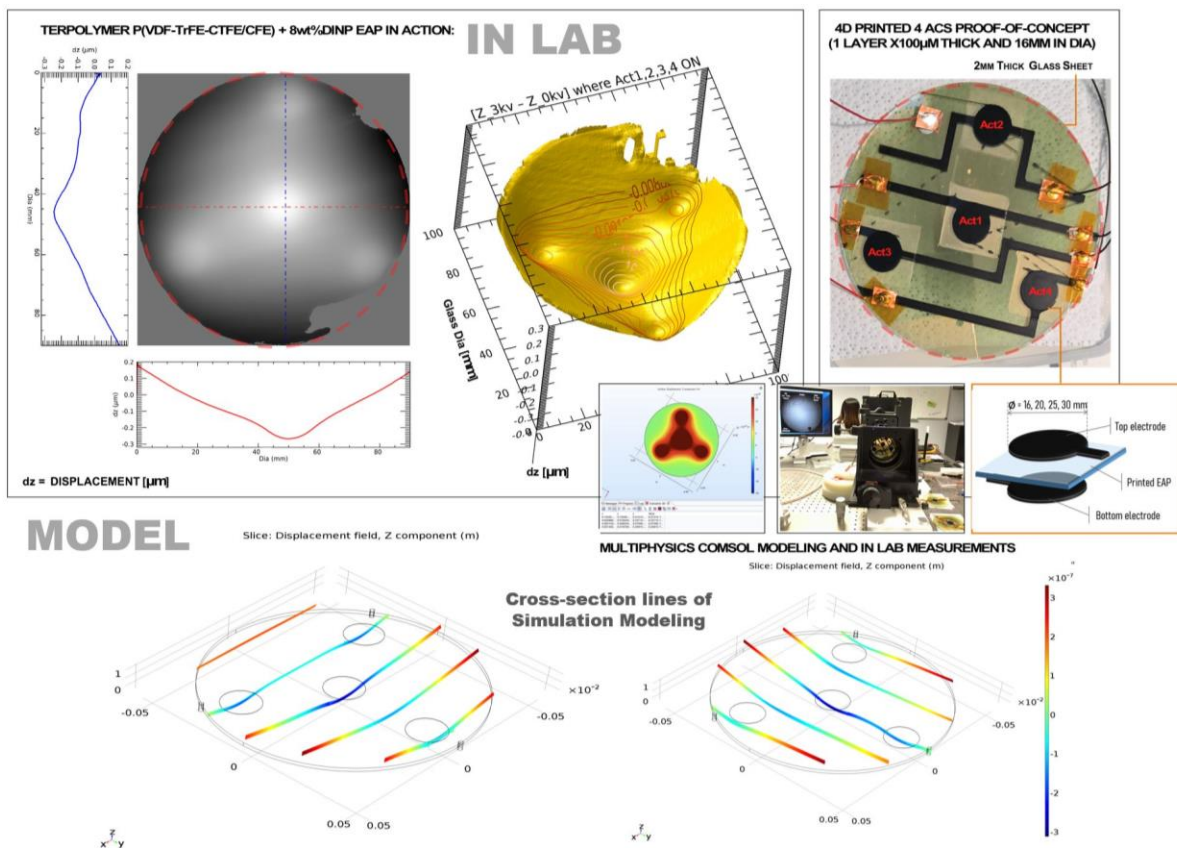
258 The full-printed actuator was prepared through a shear prototype configuration that uses the advantage
 259 of the transversal strain (S_{31}) generated by the EAP actuator. This mechanical transverse expansion creates
 260 a shear force that can shape the glass surface. After electrical polishing, the system relied on the actuator
 261 configuration. An effective electrical polishing implies high DC fields swept from 10-30 V/ μm applied
 262 directly through the electrode layers printed on the backside of the glass substrate. The control surface Sc
 263 is where the EAP force-actuators are also 3D printed in a stacked configuration (Figure 2). The Sc
 264 deformations (overall surface wavefront fringes) are measured through a laser interferometer instrument
 265 (Figure 8). These measurements are front-side reflective mirrors. The fact is that the front surface is covered
 266 by metallic deposition, while the EAP actuator is translucent and its optical properties [33,34] do not affect
 267 the mirror deformation. On one hand, the measurement was performed on the front-side mirror. This
 268 means that the incident and reflected rays driven by the Zygo interferometer appear only on the front-side
 269 of the mirror called the control surface (Sc), correspondingly. As observed in Figure 8, actuators were fixed
 270 on the backside of the mirror where the interaction with light rays is not significant. In other words, the
 271 EAP layer does not have an impact or absorb this quality of the reflective coating on the front side.
 272 Consequently, the EAP actuator was entirely operated the glass deformation without being influenced by
 273 light.



274

275 **Figure 8.** The experimental setup of the glass surface deformation presents the measurement configuration: backside, front side, and side
 276 view of the mirror prototype. The control surface: Sc (front surface) coated with gold layer was faced to the laser interferometer (Zygo
 277 Verifire™) to obtain its deformation when actuators, fixed on the backside, were actuated.

278



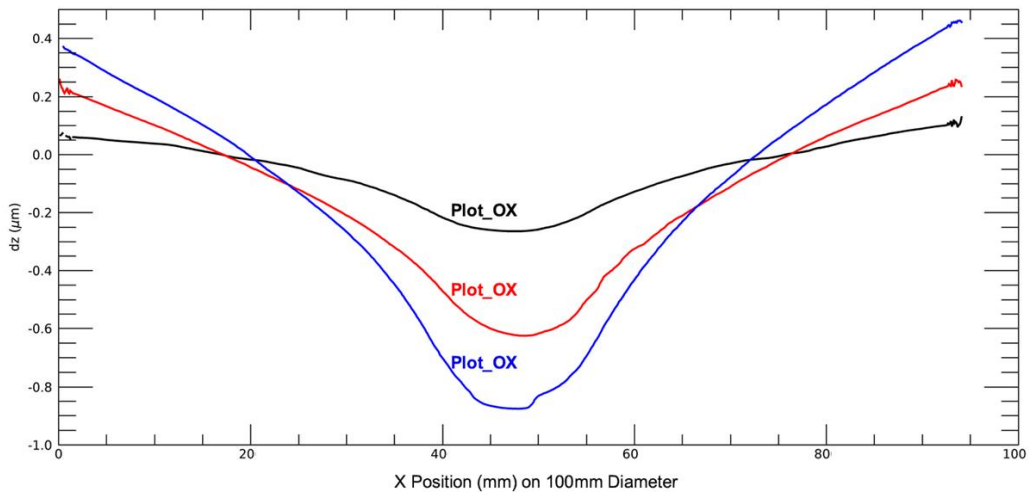
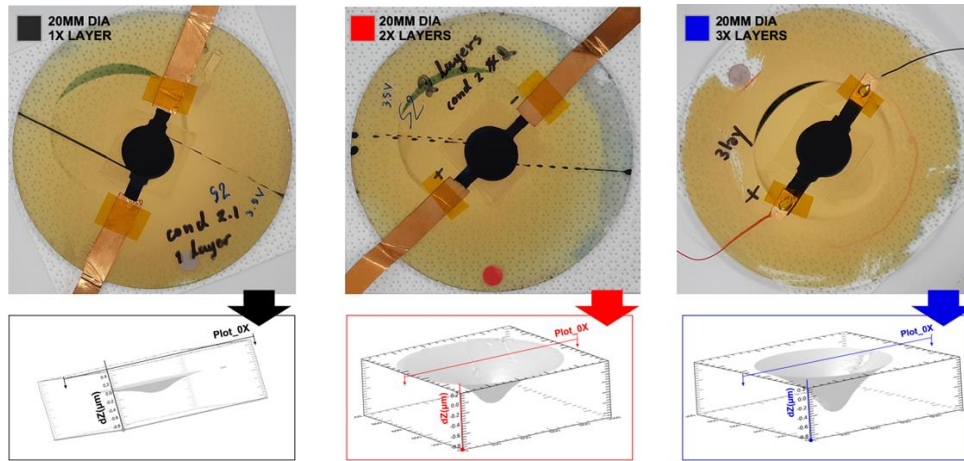
279

280 **Figure 9.** The experimental control surface: Sc (front glass) measurement of the full-printed 4-multi actuator prototype. The evaluation
 281 of surface deformation was obtained from interference fringes providing the surface plot (black and white deformation graph and 3D-surface
 282 yellow graph) accompanied by COMSOL simulation modeling that is coherent in empirical results. The float glass substrates are 110 mm
 283 in diameter and 2 mm thick. Fringe measurements are accomplished by a Fizeau-type laser interferometer (Zygo Verifire™).

284 In Figure 9, surface displacement (\mathbf{dz}) is between 0.05 to 2.00 μm during the application of an
285 electric field ($E = 30 \text{ V}/\mu\text{m}$). The electrode size (diameter and thickness) and construction configuration
286 (single layer and/or multilayer) were also measured. Figure 10 and 11 show the S_e deformation when the
287 sample was subjected to the DC voltage input. Naturally, a larger electrode and a multilayers force actuator
288 can produce larger surface deformation \mathbf{dz} . However, the multilayer structure was fabricated using the
289 shear-mode and can be limited by its number of actuator layers, which is generated by the non-transferable
290 shear force from the top layer and/or actuator interlayer clamping. This influence would make the glass
291 deformation reach a *saturation regime*. Despite that, a stronger electric field can drive the EAP actuator to
292 create higher transversal strain as well as reinforce the ability to transfer shear force from the top EAP layer
293 in the multilayer structure.

294 The shear actuator seems to deform the glass locally in consonance with its shape. Thetpraphi *et*
295 *al.* [11] has reported that dielectric permittivity as a function of an applied electric field can be modeled via
296 Debye/Langevin formalism, which enabled the possibility to predict the actuation ability of electrostrictive
297 effects in modified terpolymer composite. The success of the modeling leans on COMSOL Multiphysics®
298 software used Debye/Langevin formalism and provided impressive glass deformation modeling results
299 resembling the experimental measurement analysis (Figure 12). The spatial optimized simulation
300 corroborates the related deformation magnitude and also demonstrated harmonized cross-section
301 curvatures considering the four activated actuator prototypes (Figure 9). The appeal of these simulated and
302 experimental models (Figure 9 to 12) goes beyond scientific difficulties and carefully unravels the
303 electromechanical behavior of the terpolymer/plasticizer composite.

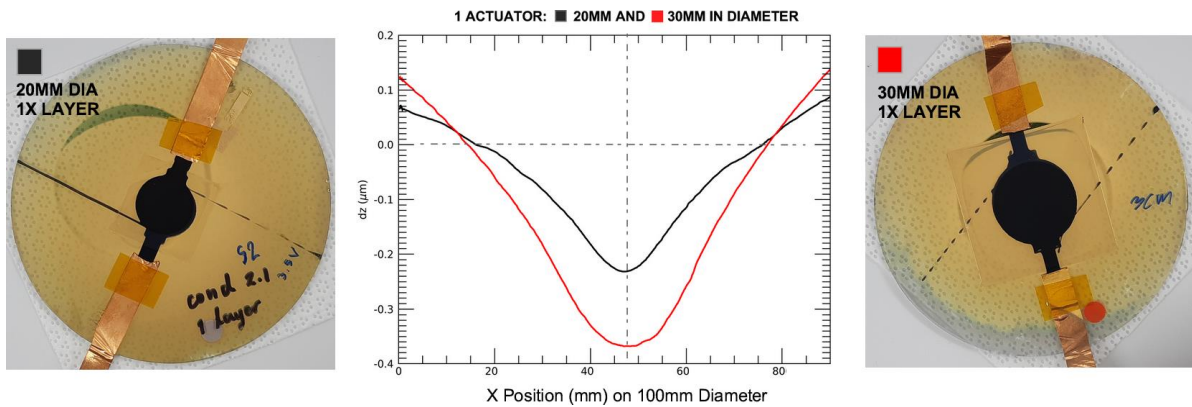
304



305

306 *Figure 10.* The control surface (S_c) deformation represents the actuated regime under a $30 \text{ V}/\mu\text{m}$ applied electric field of multilayer
 307 sample (1 actuator of 20 mm diameter) that consists of 1 layer (black), 2 layers (red), and 3 layers (blue), respectively.

308

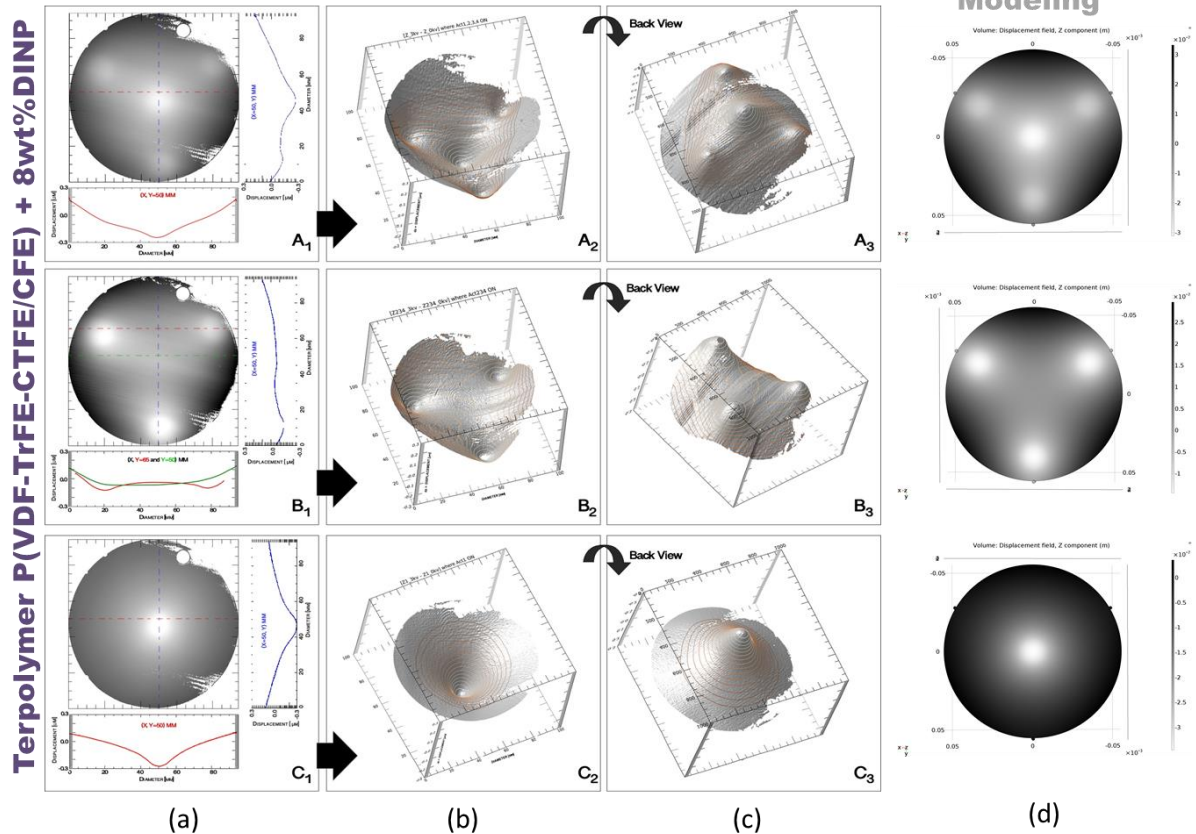


309

310 *Figure 11.* The control surface (S_c) deformation represents the actuated regime (X-cross section) under a $30 \text{ V}/\mu\text{m}$ applied electric field
 311 of a single-layer actuator prototype (1 actuator, 1 layer) with a 20 mm diameter (black) and a 30 mm diameter (red), respectively.

312

EAP IN ACTION



313

314 **Figure 12.** The control surface (S_c) deformation with their cross-section $[(X, Y), dZ]$ of the single-layer multi-actuator prototype with 16-
 315 mm-diameter electrodes driven by a $30 \text{ V}/\mu\text{m}$ electric field. Black and white illustrations show the control surface buckling comparing
 316 between experimental results and simulation models: row (a) illustrated the deformation scale plotted with their cross-section $[X, dZ]$ and
 317 $[Y, dZ]$ lines, respectively; row (b) and (c) displayed the 3D surface plot of front and backside of the control surface, respectively; and row
 318 (d) describes COMSOL simulations of glass surface deformation under similar conditions.

319

320 Table 1 shows the maximum deformation of the front glass surface generated by shear EAP to
 321 optimize the EAP sizes as well as the number of layers of the multilayer structure. Each measurement
 322 averages from 5 samples, together with the standard deviation provided in Table 1, confirming very small
 323 dispersion of the measured data. As expected, the higher displacement induces to smaller variation
 324 coefficient, i.e., defined as the SD over the mean value. This, to some extent, is reflected by the less
 325 dispersion of measures performed on the 5 tested samples when being subjected to a higher applied electric
 326 field. On the other hand, with a very low input electric field (e.g., $10 \text{ V}/\mu\text{m}$), as the samples deform very
 327 little, measurement in displacement with high precision becomes challenging. For instance, it has been
 328 pointed out in practice that for a sample of 20 mm diameter, a small displacement of $0.061 \mu\text{m}$ leads to a
 329 significant error of around 24%, while only 7.2% in the case of $0.705 \mu\text{m}$. Both experimental and modeling
 330 displacement of all prototypes depend on actuator size and number of multilayers and coincide with a range
 331 of inaccuracy measurements. Note that the surface maximum deformation in Figure 13(a) increases
 332 proportionally to an external applied electric field (E) as well as EAP actuator size (diameter & thickness).
 333 Figure 13(b) & (c) compare actuation displacements from two methods of predicting model values
 334 (COMSOL™) and measurements (maximum S_c deformation).

335 Table 1 indicated that the evaluation model results are very close to the empirical data (around 94-
 336 99%) in the case of varying electrode sizes. This small discrepancy is possibly originated from Ohmic
 337 heating because the composite electrode layer has low conductivity (high resistivity) versus an ideal
 338 conductive electrode (e.g., gold electrode). This resistive heat can indeed impact glass deformation especially
 339 in the particular case of large electrode areas having a higher amount of leakage current (Figure 13(b)).

340 The multilayer actuator has a controversy of observed displacement against the empirical model in
 341 Figure 13(c). Thetraphi *et al.* [11] reported that EAP pre-polish shear actuators can facilitate strain-
 342 generated transfer onto the glass at certain sample thicknesses. The main attribution parameters disrupting
 343 an actuation efficiency in the real-scale experiment might come from the rough interface and the stresses
 344 in the layers [35] especially the 3D printed multilayer topology. This inter-stress in multiple-layered
 345 structures impedes the effort to reinforce transferable transversal strain by increasing the number of layers.
 346 The interlayer stress algorithm of the multilayer structure must be re-optimized in future modeling to have
 347 a better accurate model prediction performance.

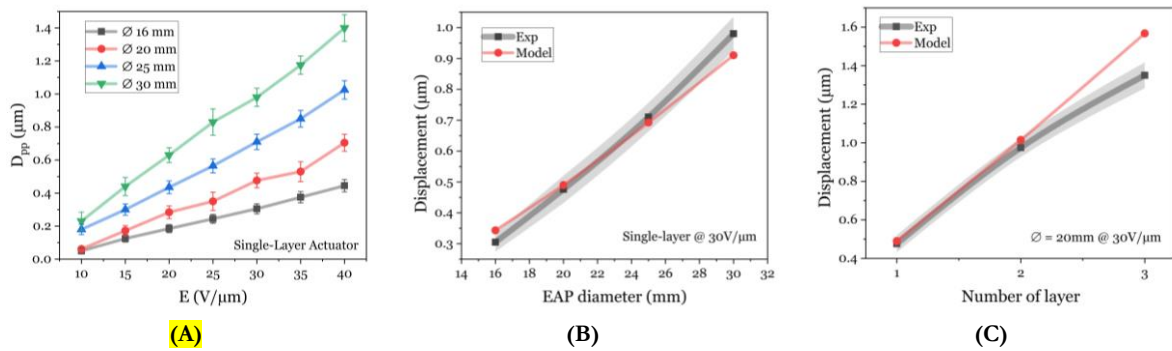
348

349 **Table 1.** The maximum displacement at the central S_c as measured by interferometric dynamic calibrator (in lab measurements) and
 350 COMSOL™ model evaluation (modelization & simulation) as a function of applied electric fields, actuator size, and the number of
 351 layers.

E (V/ μ m)	Maximum Displacement (μ m)																	
	1 layer												2 layers		3 layers			
	\varnothing 16 mm			\varnothing 20 mm			\varnothing 25 mm			\varnothing 30 mm			\varnothing 20 mm		\varnothing 20 mm			
	Exp.	$\pm \mu$ m	Model	Exp.	$\pm \mu$ m	Model	Exp.	$\pm \mu$ m	Model	Exp.	$\pm \mu$ m	Model	Exp.	$\pm \mu$ m	Model	Exp.	$\pm \mu$ m	Model
10	0.050	0.018	0.058	0.061	0.015	0.083	0.180	0.030	0.118	0.230	0.055	0.155	0.230	0.012	0.173	0.278	0.014	0.267
15	0.125	0.021		0.173	0.031		0.300	0.034		0.440	0.055		0.390	0.020		0.525	0.026	
20	0.185	0.024	0.194	0.284	0.039	0.278	0.435	0.038	0.392	0.630	0.045	0.515	0.555	0.028	0.575	0.777	0.039	0.888
25	0.244	0.027		0.350	0.055		0.565	0.042		0.830	0.080		0.745	0.037		1.010	0.051	
30	0.305	0.03	0.343	0.476	0.044	0.490	0.710	0.046	0.693	0.980	0.055	0.910	0.975	0.049	1.015	1.350	0.068	1.568
35	0.375	0.034		0.530	0.06		0.850	0.051		1.175	0.055		1.193	0.060		1.564	0.078	
40	0.445	0.037	0.475	0.705	0.051	0.678	1.025	0.056	0.959	1.400	0.080	1.260	1.493	0.075	1.405	1.838	0.092	2.170

352

353



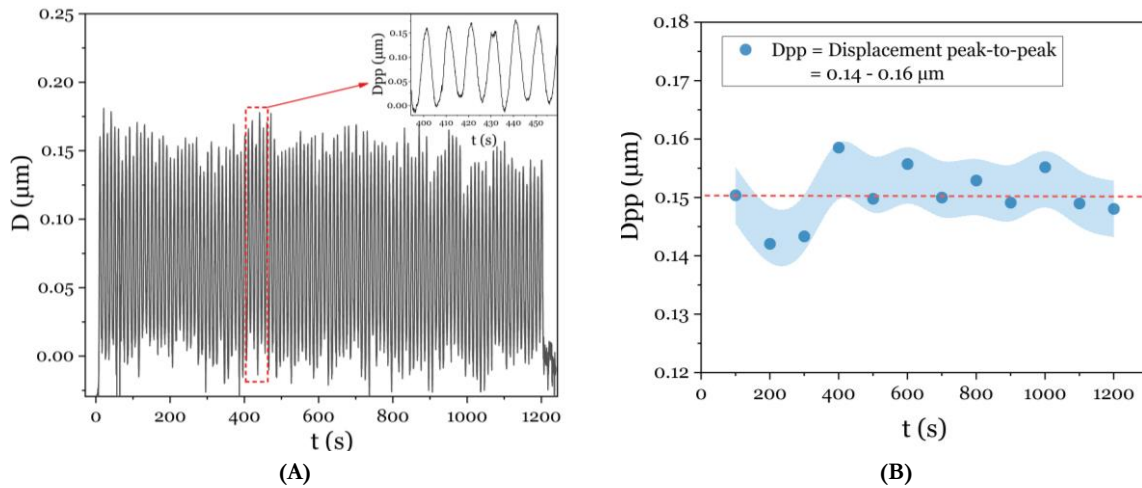
354 **Figure 13.** (A) Experimental maximum displacement as a function of electric fields of the full-printed single-layer sample with different
 355 diameter sizes. Comparison between experimental measure and modeling analysis of the same sample under a 30 V/ μ m electric field in
 356 terms of displacement versus (B) EAP diameter sizes and (C) the number of layers.

357 These results allow the assessment of this extensive actuator assembly. However, one must
 358 remember the homogeneous solvent evaporative control and stress distribution on the surface and between
 359 the interlayer and buckle delamination. Such fabrication process control is critical for an optimized
 360 mechanism. Figure 9 and Figure 12 show experimental results and confirm the compliance between
 361 electrode shape and glass optical surface deformations under an applied electric field ($E=30$ V/ μ m). Such
 362 a conclusive result paves the way for the next generation of 3D-printed multi EAP force-actuators, which

363 are a crucial part of hybrid dynamic structures for quality optical surface shape control, i.e., *electrical polishing*
364 for Live-Mirror.

365 To assess the reliable operation of the live mirror under an applied high voltage, an actuation test
366 consisting of 120 cycles was performed on a full-printed single-layer sample with a 20mm-diameter. Note
367 that this tested sample was fabricated last year and was left at room temperature for 12 months. Figure 14
368 (A) displays the time evolution of the central displacement of S_c when being subjected to an alternating
369 electric field of $15 \text{ V}/\mu\text{m}$ amplitude and 0.1 Hz frequency. As observed, the sample provided a satisfactory
370 actuation response for 20 minutes and seems to be unchanged in terms of electromechanical properties
371 even 1 year after the fabrication. The small variation of the displacement (peak-to-peak) amplitude is
372 demonstrated in Figure 14 (B). This result confirms the reliability of using the full-printed EAP actuator
373 for several actuation cycles as well as the long-time storage possible. Last but not least, the implications of
374 the physical aging of our advanced EAP actuator will be considered when assessing its long-term stability
375 under several conditions, e.g., temperature, humidity, high-frequency operation, etc.

376



377 **Figure 14.** The test of 120 actuation cycles (sinusoidal electric field of $15 \text{ V}/\mu\text{m}$, 100 mHz) on a 20mm-diameter full-printed single-
378 layer sample: (A) the real-time displacement measurement, and (B) the displacement peak-to-peak value with an area error considered as
379 the central displacement of S_c .

380

381 IV. Conclusion

382 The Live-Mirror was prototyped from lab-scale fabrication for a breakthrough in automated
383 production via additive manufacturing. The extrusion/3D printing technique underscores the feasibility of
384 scale-up in a conventional EAP fabrication process. This offers a more automatic soft actuator fabrication
385 suited for active optical applications. The printable advanced EAP and its compatible electrode (the
386 optimized terpolymer carbon black composite) led to a full-printed actuator qualifying as a Live-Mirror 3D
387 printed prototype. Modeling with COMSOL Multiphysics® showed an admirable result in excellent
388 agreement with the experimental measurements. 3D printed actuator technology could offer several
389 opportunities to create unique soft actuator applications like system controlling receiver mirrors for
390 astronomy and communication systems as well as many other modern electronic devices.

391 To enhance the electrical conductivity of the printable electrode, a new process relying on
392 dielectrophoresis of terpolymer/CB composite will be investigated, allowing to create alignment of
393 anisotropic particles. This architecture favors the electrical conduction pathway, making it possible to avoid
394 resistive self-heating under high voltage operation. Another alternative consists of using other conductive

395 particles with high shape anisotropy, such as fiber or flake shape. As a next step, the results motivate the
396 development of a hybrid electrode pattern, in which an electrical connecting path (e.g., Ag ink) linked with
397 the conductive polymer composite (CB), successfully used for a large optical area.

398 Future work will include the mirror surface combined with the particular shape of the EAP actuator
399 designed to achieve local surface correction. Simultaneously, the curvature of a glass sample without EAP
400 curvature distortion will be studied in detail to estimate the electrode and approximate the local glass
401 curvature with an EAP electrode geometry. Both experiments and models will be determined. Moreover,
402 we aim to scale up the Live-Mirror prototype for challenging real-scale receiver mirror production.

403 Acknowledgments

404 This project is sponsored by ANR (The French National Research Agency): Project #ANR-18-CE42-0007-
405 01 (Live-Mirror project). Thetraphi acknowledges the support from the DPST Thai scholarship jointly
406 administered by the Ministry of Education and the Institute for the Promotion of Teaching Science and
407 Technology Thailand, and the Franco-Thai Scholarship (2016) from Campus France. The authors thank
408 INSA-Lyon for supporting the grant to invite Prof. Jeff Kuhn and Institute Carnot for their financial
409 support. The authors also thank Asst. Prof. Chatchai Putson for assistance with Thai internships (S. Chaipo
410 and W. Kanlayakan).

411

412 References

- 413 [1] D. Grinberg, S. Siddique, M.Q. Le, R. Liang, J.F. Capsal, P.J. Cottinet, 4D Printing based piezoelectric composite for medical applications,
414 *J. Polym. Sci. Part B Polym. Phys.* 57 (2019) 109–115. <https://doi.org/10.1002/polb.24763>.
- 415 [2] Z. Xiang, V. Nguyen, B. Ducharme, N. Della Schiava, J. Capsal, P. Cottinet, M. Le, 3D Printing of Flexible Composites via
416 Magnetophoresis: Toward Medical Application Based on Low-Frequency Induction Heating Effect, *Macromol. Mater. Eng.* 2100211
417 (2021) 2100211. <https://doi.org/10.1002/mame.202100211>.
- 418 [3] S.Z. Guo, K. Qiu, F. Meng, S.H. Park, M.C. McAlpine, 3D Printed Stretchable Tactile sensors, *Adv. Mater.* 29 (2017) 1–8.
419 <https://doi.org/10.1002/adma.201701218>.
- 420 [4] O.F. Emon, F. Alkadi, D.G. Philip, D. Kim, K. Lee, Multi-material 3D printing of a soft pressure sensor, *Addit. Manuf.* 28 (2019) 629–
421 638. <https://doi.org/10.1016/j.addma.2019.06.001>.
- 422 [5] V.C.F. Li, C.K. Dunn, Z. Zhang, Y. Deng, H.J. Qi, Direct Ink Write (DIW) 3D Printed Cellulose Nanocrystal Aerogel Structures, *Sci.*
423 *Rep.* 7 (2017) 1–8. <https://doi.org/10.1038/s41598-017-07771-y>.
- 424 [6] S.H. Park, R. Su, J. Jeong, S.Z. Guo, K. Qiu, D. Joung, F. Meng, M.C. McAlpine, 3D Printed Polymer photodetectors, *Adv. Mater.* 30
425 (2018) 1–8. <https://doi.org/10.1002/adma.201803980>.
- 426 [7] G. Haghiashtiani, E. Habtour, S.H. Park, F. Gardea, M.C. McAlpine, 3D printed electrically-driven soft actuators, *Extrem. Mech. Lett.*
427 21 (2018) 1–8. <https://doi.org/10.1016/j.eml.2018.02.002>.
- 428 [8] B. Sparrman, C. Pasquier, S. Darbari, R. Rustom, K. Shea, S. Tibbits, Printed silicone pneumatic actuators for soft robotics, *Addit. Manuf.*
429 (2021) 101860. <https://doi.org/10.1016/j.addma.2021.101860>.
- 430 [9] Additive manufacturing, *GE Addit.* (2019). <https://www.ge.com/additive/additive-manufacturing> (accessed May 8, 2019).
- 431 [10] K. Thetraphi, M.Q. Le, A. Houachti, P. Cottinet, L. Petit, D. Audigier, J. Kuhn, G. Moretto, J. Capsal, Surface Correction Control
432 Based on Plasticized Multilayer P(VDF-TrFE-CFE) actuator—Live Mirror, *Adv. Opt. Mater.* 1900210 (2019) 1900210.
433 <https://doi.org/10.1002/adom.201900210>.
- 434 [11] K. Thetraphi, S. Chaipo, W. Kanlayakan, P.-J. Cottinet, M.Q. Le, L. Petit, D. Audigier, J. Kuhn, G. Moretto, J.-F. Capsal, Advanced
435 Plasticized Electroactive Polymers Actuators for Active Optical Applications: Live Mirror, *Adv. Eng. Mater.* 22 (2020) 1901540.
- 436 [12] Hyrel 3D, Hyrel 3D SYSTEM 30M, (2019). <http://www.hyrel3d.com/portfolio/system-30m/> (accessed February 24, 2020).
- 437 [13] S.C. Ligon, R. Liska, J. Stampfl, M. Gurr, R. Mülhaupt, Polymers for 3D Printing and Customized Additive Manufacturing, *Chem. Rev.*
438 117 (2017) 10212–10290. <https://doi.org/10.1021/acs.chemrev.7b00074>.
- 439 [14] A.L. Dearden, P.J. Smith, D. Shin, N. Reis, B. Derby, P.O. Brien, A low curing temperature silver ink for use in ink-jet printing and
440 subsequent production of conductive tracks, *Macromol. Rapid Commun.* 26 (2005) 315–318. <https://doi.org/10.1002/marc.200400445>.
- 441 [15] L. V Kayser, M.D. Russell, D. Rodriguez, S.N. Abuhamdieh, C. Dhong, S. Khan, A.N. Stein, J. Ram, D.J. Lipomi, RAFT Polymerization
442 of an Intrinsically Stretchable Water-Soluble Block Copolymer Scaffold for PEDOT, *Chem. Mater.* 30 (2018) 4459–4468.

443 <https://doi.org/10.1021/acs.chemmater.8b02040>.

444 [16] C. Cochrane, V. Koncar, M. Lewandowski, C. Dufour, Design and Development of a Flexible Strain Sensor for Textile Structures Based
445 on a Conductive Polymer Composite, *Sensors*. 7 (2007) 473–492.

446 [17] N. Kumar, P.K. Jain, P. Tandon, P.M. Pandey, Additive manufacturing of flexible electrically conductive polymer composites via CNC-
447 assisted fused layer modeling process, *J. Brazilian Soc. Mech. Sci. Eng.* 40 (2018) 175. <https://doi.org/10.1007/s40430-018-1116-6>.

448 [18] A. Materials, Float Glass - Properties and Applications, (n.d.). <https://www.azom.com/properties.aspx?ArticleID=89> (accessed May 6,
449 2021).

450 [19] K. Thetraphi, G. Moretto, J.R. Kuhn, P.-J. Cottinet, M.Q. Le, D. Audigier, L. Petit, J. Capsal, Live-mirror shape correction technology
451 operated through modified electroactive polymer actuators, *Proc. SPIE*. (2019). <https://doi.org/10.1117/12.2514229>.

452 [20] G. Cummins, M.P. Desmulliez, Inkjet printing of conductive materials: a review, *Circuit World*. (2012).
453 <https://doi.org/10.1108/03056121211280413>.

454 [21] N. Della Schiava, K. Thetraphi, M.Q. Le, P. Lermusiaux, A. Millon, J.-F. Capsal, P.-J. Cottinet, Enhanced figures of merit for a high-
455 performing actuator in electrostrictive materials, *Polymers (Basel)*. 10 (2018) 1–15. <https://doi.org/10.3390/polym10030263>.

456 [22] J.-F. Capsal, J. Galineau, M. Lallart, P.-J. Cottinet, D. Guyomar, Plasticized relaxor ferroelectric terpolymer: Toward giant electrostriction,
457 high mechanical energy and low electric field actuators, *Sensors Actuators, A Phys.* 207 (2014) 25–31.
458 <https://doi.org/10.1016/j.sna.2013.12.008>.

459 [23] X. Yin, J.-F. Capsal, D. Guyomar, A comprehensive investigation of poly(vinylidene fluoride- trifluoroethylene-chlorofluoroethylene)
460 terpolymer nanocomposites with carbon black for electrostrictive applications, *Appl. Phys. Lett.* 104 (2014) 2012–2017.
461 <https://doi.org/10.1063/1.4864160>.

462 [24] N. Della Schiava, M.Q. Le, J. Galineau, F. Domingues Dos Santos, P.-J. Cottinet, J.-F. Capsal, Influence of Plasticizers on the
463 Electromechanical Behavior of a P(VDF-TrFE-CTFE) Terpolymer: Toward a High Performance of Electrostrictive Blends, *J. Polym.*
464 *Sci. Part B Polym. Phys.* 55 (2017) 355–369. <https://doi.org/10.1002/polb.24280>.

465 [25] X. Yin, Modification of Electrostrictive Polymers and Their Electromechanical Applications, INSA de Lyon, 2015.

466 [26] M. Rahaman, A. Aldalbah, P. Govindasami, N. Khanam, S. Bhandari, P. Feng, T. Altalhi, A New Insight in Determining the Percolation
467 Threshold of Electrical Conductivity for Extrinsicly Conducting Polymer Composites through Different sigmoidal models, *Polymers*
468 (Basel). 10 (2017) 527. <https://doi.org/10.3390/polym9100527>.

469 [27] Q. Zhang, J. Wang, B. Zhang, B. Guo, J. Yu, Z. Guo, Improved electrical conductivity of polymer/carbon black composites by
470 simultaneous dispersion and interaction-induced network assembly, *Compos. Sci. Technol.* 179 (2019) 106–114.
471 <https://doi.org/10.1016/j.compscitech.2019.05.008>.

472 [28] K. Thetraphi, Development of electroactive polymer actuators for next generation mirror : Live-Mirror, Université de Lyon, 2020.

473 [29] F. Kremer, S. Andreas, Broadband Dielectric Measurement Techniques, Springer Science & Business Media, 2002.

474 [30] A. Kahouli, Spectroscopie diélectrique appliquée aux polymères, Tech. l'ingénieur Matériaux Isolants En Électrotechnique. TIB255DUO
475 (2016). [https://www.techniques-ingenieur.fr/base-documentaire/energies-th4/materiaux-isolants-en-electrotechnique-
476 42255210/spectroscopie-dielectrique-appliquee-aux-polymeres-d2308/](https://www.techniques-ingenieur.fr/base-documentaire/energies-th4/materiaux-isolants-en-electrotechnique-42255210/spectroscopie-dielectrique-appliquee-aux-polymeres-d2308/).

477 [31] J.-F. Capsal, J. Galineau, M.Q. Le, F. Domingues Dos Santos, P.-J. Cottinet, Enhanced electrostriction based on plasticized relaxor
478 ferroelectric P(VDF-TrFE-CFE/CTFE) blends, *J. Polym. Sci. Part B Polym. Phys.* 53 (2015) 1368–1379.
479 <https://doi.org/10.1002/polb.23776>.

480 [32] F. Pedroli, A. Marrani, M.Q. Le, O. Sanseau, P.-J. Cottinet, J.-F. Capsal, Reducing leakage current and dielectric losses of electroactive
481 polymers through electro-annealing for high-voltage actuation, *RSC Adv.* 9 (2019) 12823–12835. <https://doi.org/10.1039/c9ra01469a>.

482 [33] M. Ben-David, L. Engel, Y. Shacham-Diamand, Spectroscopic ellipsometry study of spin coated P(VDF-TrFE-CTFE) thin films and
483 P(VDF-TrFE-CTFE)/PMMA blends, *Microelectron. Eng.* 171 (2017) 37–43. <https://doi.org/10.1016/j.mee.2017.01.030>.

484 [34] D. Jeong, Electro-Optical Properties in Relaxor Ferroelectric Materials and the Device Applications, (2004) 125.

485 [35] S. Faulhaber, C. Mercer, M.-W. Moon, J. Hutchinson, A. Evans, Buckling delamination in compressed multilayers on curved substrates
486 with accompanying ridge cracks, *J. Mech. Phys. Solids*. 54 (2006) 1004–1028. <https://doi.org/10.1016/j.jmps.2005.11.005>.

487